

1988

Integrable and Nonintegrable Classical Spin Clusters: Trajectories and Geometric Structure of Invariants

Niraj Srivastava

Charles Kaufman

University of Rhode Island, ckaufman@uri.edu

Gerhard Müller

University of Rhode Island, gmuller@uri.edu

R Weber

H. Thomas

Follow this and additional works at: https://digitalcommons.uri.edu/phys_facpubs

Citation/Publisher Attribution

Srivastava, N., Kaufman, C., Muller, G., Weber, R., & Thomas, H. (1988). Integrable and nonintegrable classical spin clusters: trajectories and geometric structure of invariants. *Zeitschrift für Physik B Condensed Matter*, 70, 251-268.

Available at: <http://dx.doi.org/10.1007/BF01318307>

This Article is brought to you by the University of Rhode Island. It has been accepted for inclusion in Physics Faculty Publications by an authorized administrator of DigitalCommons@URI. For more information, please contact digitalcommons-group@uri.edu. For permission to reuse copyrighted content, contact the author directly.

Integrable and Nonintegrable Classical Spin Clusters: Trajectories and Geometric Structure of Invariants

Terms of Use

All rights reserved under copyright.

Integrable and nonintegrable classical spin clusters: trajectories and geometric structure of invariants

N. Srivastava,¹ C. Kaufman,¹ G. Müller,¹ R. Weber,² and H. Thomas²

¹ *Department of Physics, University of Rhode Island, Kingston RI 02881, USA*

² *Institut für Physik, Universität Basel, Switzerland*

This study investigates the nonlinear dynamics of a pair of exchange-coupled spins with biaxial exchange and single-site anisotropy. It represents a Hamiltonian system with 2 degrees of freedom for which we have already established the (nontrivial) integrability criteria and constructed the integrals of the motion provided they exist. Here we present a comparative study of the phase-space trajectories for two specific models with the same symmetry properties, one of which (the XY model with exchange anisotropy) is integrable, and the other (the XY model with single-site anisotropy) nonintegrable. In the integrable model, the integrals of the motion (analytic invariants) can be reconstructed numerically by means of time averages of dynamical variables over all trajectories. In the nonintegrable model, such time averages over trajectories define nonanalytic invariants, where the nonanalyticities are associated with the presence of chaotic trajectories. A prominent feature in the nonintegrable model is the occurrence of very long time scales caused by the presence of low-flux cantori, which form "sticky" coats on the boundary between chaotic regions and regular islands or "leaky" walls between different chaotic regions. These cantori dominate the convergence properties of time averages and presumably determine the long-time asymptotic properties of dynamic correlation functions. Finally, we present a special class of integrable systems containing arbitrarily many spins coupled by general biaxial exchange anisotropy.

I. INTRODUCTION

This is the second paper of a projected series on the dynamical properties of integrable and nonintegrable classical spin clusters. In the first paper [1], we examined in detail the problem of integrability of a pair of exchange-coupled classical spins with biaxial exchange and single-site anisotropy. It represents the simplest autonomous spin system for which the integrability problem is nontrivial. We found that such a system is completely integrable only if the model parameters satisfy a certain condition. For the integrable cases, the second integral of the motion (in addition to the Hamiltonian), which guarantees integrability, was determined explicitly.

Whereas [1] emphasized the integrability criteria and the analytic structure of invariants, the focus of the present paper is the study of the geometric structure of invariants, i.e. of analytic invariants in integrable cases and of nonanalytic invariants in nonintegrable cases [2]. A study of this kind must include an investigation of the nature and the properties of phase-space trajectories for integrable and for nonintegrable cases, given the fact that invariants can be determined as time averages of dynamical variables along trajectories. A further objective of this paper is to prepare the ground for the third paper of this series, which will report a study of time-dependent correlation functions for classical spin clusters.

The results of the present study should be viewed not only in the context of chaos in classical Hamiltonian systems, which continues to challenge researchers with important unresolved issues, but also in the context of quantum chaos, which has triggered considerable excitement recently in theoretical and experimental physics [3]. As was pointed out in a recent conceptual study [4], the various aspects of chaos in classical and quantum Hamil-

tonian systems can conveniently be investigated and put in relation to one another, by studying models of N interacting quantum spins, each with quantum number s , either in the classical limit: N finite, $s \rightarrow \infty$, or in the thermodynamic limit: s finite, $N \rightarrow \infty$.

Finally, in a materials science context, spin clusters feature prominently in a variety of compounds [5, 6], and spin cluster models play a crucial role in the study of magneto-structural correlations, i.e. in the study of the relationship between the observed magnetic properties of a material and its chemical and structural characteristics [7], particularly in studies of the nature of superexchange interactions [5].

II. INTEGRABILITY CONDITIONS FOR CLASSICAL SPIN CLUSTERS

Consider a system of N localized classical three-component spins \mathbf{S}_l , $l = 1, \dots, N$ specified by some interaction Hamiltonian $H(\mathbf{S}_1, \dots, \mathbf{S}_N)$. Its time evolution is governed by the equation of motion

$$d\mathbf{S}_l/dt = \{H, \mathbf{S}_l\}, \quad l = 1, \dots, N. \quad (\text{II.1})$$

The Poisson brackets for classical spin variables (the symplectic structure for classical spin dynamics) are constructed via the condition that the \mathbf{S}_l are angular momentum vectors:

$$\{S_l^\alpha, S_{l'}^\beta\} = -\delta_{ll'} \sum_\gamma \epsilon^{\alpha\beta\gamma} S_l^\gamma. \quad (\text{II.2})$$

This guarantees that the Hamilton equation of motion (II.1) is consistent with the Heisenberg equation of motion for quantum spin operators. If the classical spins \mathbf{S}_l

are expressed in terms of spherical coordinates as

$$\mathbf{S}_l = S(\sin \vartheta_l \cos \phi_l, \sin \vartheta_l \sin \phi_l, \cos \vartheta_l) \quad (\text{II.3})$$

then a set of canonical variables is given by $p_l = S \cos \vartheta_l, q_l = \phi_l$. Therefore, a system of N classical spins specified by an energy function $H(\mathbf{S}_1, \dots, \mathbf{S}_N)$ represents an autonomous Hamiltonian system of N degrees of freedom. The system is completely integrable if there exist N distinct integrals of the motion in involution:

$$I_k(\mathbf{S}_1, \dots, \mathbf{S}_N) = \text{const}, \quad k = 1, \dots, N \quad (\text{II.4})$$

with $\{I_k, I_{k'}\} = 0$ for $k, k' = 1, \dots, N$.

In [1] we have studied the integrability problem for a system of two exchange-coupled spins, specified by a Hamiltonian of the general form

$$H = \sum_{\alpha=xyz} \left\{ -J_\alpha S_1^\alpha S_2^\alpha + \frac{1}{2} A_\alpha [(S_1^\alpha)^2 + (S_2^\alpha)^2] \right\} \quad (\text{II.5})$$

which includes both exchange and single-site anisotropy. We have shown that an independent integral of the motion (in addition to H) quadratic in the spin variables exists if and only if the model constants satisfy the equation

$$(A_x - A_y)(A_y - A_z)(A_z - A_x) + \sum_{\alpha\beta\gamma=\text{cycl}(xyz)} J_\alpha^2 (A_\beta - A_\gamma) = 0. \quad (\text{II.6})$$

If $A_x = A_y = A_z$, the second invariant has the form

$$I = - \sum_{\alpha\beta\gamma=\text{cycl}(xyz)} J_\alpha J_\beta S_1^\alpha S_2^\beta + \frac{1}{2} \sum_{\alpha=xyz} J_\alpha^2 [(S_1^\alpha)^2 + (S_2^\alpha)^2]. \quad (\text{II.7})$$

If not all three A_α , are equal, it is given by

$$I = \sum_{\alpha=xyz} g_\alpha S_1^\alpha S_2^\alpha, \quad (\text{II.8})$$

$$g_\alpha = J_\alpha(J_\alpha + J_\beta + J_\gamma) + (A_\alpha - A_\beta)J_\gamma + (A_\alpha - A_\gamma)J_\beta - (A_\alpha - A_\beta)(A_\alpha - A_\gamma) \quad (\text{II.9})$$

with $\alpha\beta\gamma = \text{cycl}(xyz)$. Moreover, we have provided numerical evidence that the violation of condition (II.6) implies not only the nonexistence of a quadratic invariant but the nonexistence of a second independent analytic invariant in general.

For the case of pure exchange anisotropy ($A_x = A_y = A_z = 0$), it can be readily shown that the property of complete integrability extends to clusters of more than 2 spins, in fact, to a special class of clusters with arbitrarily many spins. Let us rewrite the integrable 2-spin Hamiltonian (II.5) for $A_x = A_y = A_z = 0$ in the form

$$H^{(2)} = -\mathbf{S}_1 \cdot J \cdot \mathbf{S}_2, \quad J_{\alpha\beta} = J_\alpha \delta_{\alpha\beta}. \quad (\text{II.10})$$

Now consider the N -spin Hamiltonian characterized by the same type of anisotropic bilinear exchange interaction

$$H^{(N)} = -\mathbf{T}_A \cdot J \cdot \mathbf{T}_B = - \sum_{l \in A} \sum_{l' \in B} \mathbf{S}_l \cdot J \cdot \mathbf{S}_{l'} \quad (\text{II.11})$$

where

$$\mathbf{T}_A = \sum_{l \in A} \mathbf{S}_l, \quad \mathbf{T}_B = \sum_{l' \in B} \mathbf{S}_{l'}. \quad (\text{II.12})$$

It represents a model consisting of two arrays of spins, A and B , such that all N_A spins of array A interact with each of the $N_B = N - N_A$ spins of array B , but spins belonging to the same array do not interact directly. This class includes the case of a two-sublattice antiferromagnet with constant inter-sublattice and zero intra-sublattice coupling. Hamiltonian (II.11) describes an effective 2-spin system consisting of the two array-spins \mathbf{T}_A and \mathbf{T}_B whose equations of motion read:

$$\dot{\mathbf{T}}_A = \mathbf{T}_A \times (J \cdot \mathbf{T}_B), \quad \dot{\mathbf{T}}_B = \mathbf{T}_B \times (J \cdot \mathbf{T}_A). \quad (\text{II.13})$$

This system is integrable, for it is equivalent to the model (II.5) with $A_x = A_y = A_z = 0$ and $\mathbf{S}_1 \equiv \mathbf{T}_A, \mathbf{S}_2 \equiv \mathbf{T}_B$ now representing spins of generally unequal length. Explicit solutions for special cases of this model will be discussed in Sect. III. For given solutions $\mathbf{T}_A(t)$ and $\mathbf{T}_B(t)$, the time evolution of the individual spins \mathbf{S}_l is then governed by a set of *linear* and *decoupled* vector equations,

$$\dot{\mathbf{S}}_l = \mathbf{S}_l \times (J \cdot \mathbf{T}_B(t)), \quad l \in A, \quad (\text{II.14})$$

each one representing the motion of a single spin \mathbf{S}_l of array A in a time-dependent external field $\mathbf{h}(t) = J \cdot \mathbf{T}_B(t)$, and correspondingly for $A \leftrightarrow B$.

A complete set of N independent integrals of the motion in involution for this system consists of two invariants which govern the time evolution of the two vectors \mathbf{T}_A and \mathbf{T}_B and of $N - 2 = (N_A - 1) + (N_B - 1)$ invariants which govern the time evolution of the individual spins in arrays A and B . The first two invariants are the effective 2-spin Hamiltonian $H^{(N)}$, (II.11), and its second invariant (II.7) with \mathbf{S}_1 and \mathbf{S}_2 replaced by \mathbf{T}_A and \mathbf{T}_B , respectively. The remaining $N - 2$ invariants can be selected as follows:

$$I_l^A = \mathbf{S}_l \cdot \sum_{k \in A < l} \mathbf{S}_k, \quad l \in A = 2, \dots, N_A \quad (\text{II.15})$$

and $A \leftrightarrow B$. These latter invariants ensure the fixed length of the vectors \mathbf{T}_A and \mathbf{T}_B . In fact, all scalar products $\mathbf{S}_l \cdot \mathbf{S}_{l'}$, of spins belonging to the same array A or B are conserved. Since the number of independent scalar products is $(2N_A - 3) + (2N_B - 3) = 2N - 6$, there are – together with (II.11) and (II.7) – at least $2N - 4$ independent invariants. This reduces the maximum number of independent frequencies to 4, irrespective of the size of arrays A and B .

It is interesting to compare this result with that for another class of completely integrable N -spin systems: the “complete clusters”, where every spin is coupled to every other spin by a uniform isotropic exchange interaction (Kittel-Shore model)

$$H = -\frac{1}{2} \sum_{l \neq l'} \mathbf{S}_l \cdot \mathbf{S}_{l'}. \quad (\text{II.16})$$

This model possesses $2N - 1$ independent invariants [8] and, therefore, only a single frequency in its time evolution, which characterizes the precession of every spin about the direction of the total spin, as discussed in [1].

The first column of Fig. 1 shows the spin clusters containing up to $N = 6$ spins which are integrable for general anisotropic bilinear exchange interaction. The second column shows those spin clusters which are integrable only for fully isotropic exchange interaction. The third column, finally, shows some of the remaining types of clusters for these values of N , which are presumably nonintegrable [9]. Some noteworthy observations are the following: The closed chain of 3 spins coupled by isotropic exchange interaction (integrable) and uniaxially anisotropic exchange interaction (nonintegrable) was previously studied in some detail [10]. It is interesting to note that by breaking one of the 3 bonds the system turns integrable even for biaxial exchange anisotropy. This is in strong contrast to the 4-spin cluster: here the closed chain is integrable for the most general (biaxially anisotropic) interaction, but the open chain is nonintegrable even for the most symmetric interaction. Consider

N	I	II	III
2		—	—
3			—
4			
5			
6			

FIG. 1: Classical spin clusters containing up to $N = 6$ spins which are integrable for arbitrary exchange anisotropy (column I), clusters which are integrable only for isotropic exchange interactions (II) and clusters which are presumably nonintegrable for any type of bilinear interaction (III)

a complete cluster for arbitrary even N . It is integrable for isotropic Heisenberg coupling but turns nonintegrable in the presence of uniaxial or biaxial exchange anisotropy. Integrability is restored, however, by breaking roughly half of the bonds.

III. THE XY MODEL WITH EXCHANGE ANISOTROPY: AN INTEGRABLE MODEL

A special case of the general classical two-spin model (II.5) for which dynamical integrability was established in [1] is the XY model with exchange anisotropy, described by the Hamiltonian

$$H_\gamma = -(1 + \gamma)S_1^x S_2^x - (1 - \gamma)S_1^y S_2^y. \quad (\text{III.1})$$

The two integrals of the motion which guarantee integrability are the energy

$$E \equiv H_\gamma = \text{const} \quad (\text{III.2})$$

and the function

$$I \equiv (1 + \gamma)^2 [(S_1^x)^2 + (S_2^x)^2] + (1 - \gamma)^2 [(S_1^y)^2 + (S_2^y)^2] - 2(1 - \gamma^2)S_1^z S_2^z = \text{const}. \quad (\text{III.3})$$

For the two special cases $\gamma = 0$ (isotropic XY model) and $\gamma = 1$ (Ising model), a second integral of the motion is guaranteed by the conservation of the component of the total spin along the symmetry axis:

$$M_z \equiv \frac{1}{2}(S_1^z + S_2^z) = \text{const} \quad (\gamma = 0) \quad (\text{III.4})$$

$$M_x \equiv \frac{1}{2}(S_1^x + S_2^x) = \text{const} \quad (\gamma = 1). \quad (\text{III.5})$$

In fact the two general invariants E and I can be combined to a new second invariant,

$$\begin{aligned} I' &\equiv I - 4\gamma E \\ &= 2\gamma(1 + \gamma)(S_1^x + S_2^x)^2 - (1 - \gamma^2)(S_1^z + S_2^z)^2 \\ &\quad - 2\gamma(1 - \gamma)(S_1^y - S_2^y)^2 + 2(1 - \gamma^2) = \text{const} \end{aligned} \quad (\text{III.6})$$

which reduces to a quadratic function of M_z or M_x in the two limits $\gamma = 0$ and $\gamma = 1$, respectively. In the following, we analyze the spin motion of this integrable spin model for cases of increasing complexity. The results will then be compared (in Sect. 4) with corresponding results for the spin motion of a nonintegrable spin model which has the same symmetry properties.

A. Trajectories for $\gamma = 1$: simple precession

The Ising limit $\gamma = 1$ is the only case for which the equations of motion of the model H_γ , (III.1), are effectively linear. We have

$$\dot{S}_1^x = 0, \quad \dot{S}_1^y = 2S_1^z S_2^x, \quad \dot{S}_1^z = -2S_1^y S_2^x \quad (\text{III.7})$$

and $1 \leftrightarrow 2$ with the simple solution

$$(S_1^x, S_1^y, S_1^z) = S(\cos \beta_1, \sin \beta_1 \sin(\omega_1 t + \psi_1), \sin \beta_1 \cos(\omega_1 t + \psi_1)) \quad (\text{III.8})$$

where

$$\omega_1 = 2 \cos \beta_2 \quad (\text{III.9})$$

and $1 \leftrightarrow 2$ ($\beta_{1,2}$ and $\psi_{1,2}$ are constants of integration). Thus both spins precess uniformly about the symmetry axis, and the precession frequency of one spin depends on the (constant) angle of the other spin with respect to that axis. This explicit dynamical solution is readily generalized to an "Ising model"

$$H = - \sum_{ij} J_{ij} S_i^x S_j^x \quad (\text{III.10})$$

on an arbitrary lattice. The precession frequency of any spin then depends on the (constant) angles with respect to the symmetry axis of all spins with which this spin is coupled. The simplicity of the dynamics of this model is related to the fact that the time evolution of any particular spin depends only on the *initial conditions* of the spins with which it is coupled, but not on their *time evolution*. Hence, this model does not support any collective modes.

B. Trajectories for $\gamma = 0$: particle in a one-dimensional potential

In the isotropic limit $\gamma = 0$ of H_γ , the time evolution of the two spins is strongly coupled. The equations of motion can nevertheless be solved explicitly as outlined in the following. In terms of the spherical coordinates (II.3) we have four independent equations of motion of the form

$$\begin{aligned} \dot{\vartheta}_1 &= \sin \vartheta_2 \sin(\phi_1 - \phi_2), \\ \dot{\phi}_1 &= \cot \vartheta_1 \sin \vartheta_2 \cos(\phi_1 - \phi_2) \end{aligned} \quad (\text{III.11})$$

and $1 \leftrightarrow 2$ determining the time evolution of $H_{\gamma=0}$. Introducing two new variables

$$z = \frac{1}{2}(\cos \vartheta_1 - \cos \vartheta_2), \quad \zeta = \tan(\phi_1 - \phi_2) \quad (\text{III.12})$$

and making use of the two integrals of the motion

$$E = -\sin \vartheta_1 \sin \vartheta_2 \cos(\phi_1 - \phi_2) = \text{const} \quad (\text{III.13})$$

$$M_z = \frac{1}{2}(\cos \vartheta_1 + \cos \vartheta_2) = \text{const} \quad (\text{III.14})$$

we can combine (III.11) to a closed set of two equations

$$\dot{z} = E\zeta, \quad \dot{\zeta} = -\frac{2z}{E}(1 + M_z^2 - z^2) \quad (\text{III.15})$$

which in turn can be formulated as Newton's equation of motion

$$\ddot{z} = -2z(1 + M_z^2 - z^2) \equiv -V'(z) \quad (\text{III.16})$$

for a fictitious particle of unit mass in a 1D anharmonic potential

$$V(z) = (1 + M_z^2)z^2 - \frac{1}{2}z^4. \quad (\text{III.17})$$

This potential, which is depicted in Fig. 2, has the form of an inverted double well. It is useful to introduce a new integral of the motion, the particle energy:

$$U(E, M_z) = \frac{1}{2}\dot{z}^2 + V(z) = \frac{1}{2}[(1 - M_z^2)^2 - E^2]. \quad (\text{III.18})$$

The mapping to the spin problem imposes the constraints

$$1 - M_z^2 \leq |E| \leq 1 \quad (\text{III.19})$$

on the constants E and M_z . The potential problem is then readily solved in terms of Jacobi elliptic functions:

$$\begin{aligned} z(t) &= z_0 \text{sn}\left(at, \frac{z_0}{a}\right), \\ \zeta(t) &= \frac{az_0}{E} \text{cn}\left(at, \frac{z_0}{a}\right) \text{dn}\left(at, \frac{z_0}{a}\right) \end{aligned} \quad (\text{III.20})$$

where

$$a = \left[1 + M_z^2 + \sqrt{4M_z^2 + E^2}\right]^{1/2} \quad (\text{III.21})$$

is a constant and

$$z_0 = \left[1 + M_z^2 - \sqrt{4M_z^2 + E^2}\right]^{1/2} \quad (\text{III.22})$$

is the maximum displacement of the fictitious particle for a given energy $U(E, M_z)$. The function $z(t)$ provides

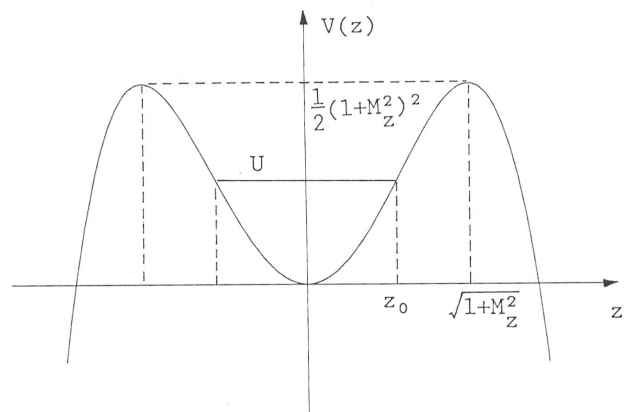


FIG. 2: Anharmonic potential $V(z)$ given by (III.17). The maximum displacement of the particle is $|z_0| = 1$ and its maximum energy is $U = 1/2$; both values are realized for $E = M_z = 0$. Shown is the curve for $M_z = 1/2$.

(in conjunction with the invariant (III.14)) a complete description of the meridional motion of the two spins. In order to complete the description of the spin motion, we have to supplement the function $\zeta(t)$, which characterizes the relative azimuthal motion of the two spins, by the overall precessional motion of the spins about the z -axis. It is readily found that this motion can also be expressed in terms of the solutions (III.20), namely through the relation

$$\dot{\Phi} = \frac{d}{dt} \frac{1}{2}(\phi_1 + \phi_2) = -\frac{M_z}{E} \frac{1 - M_z^2 + z^2(t)}{1 + \zeta^2(t)}. \quad (\text{III.23})$$

Note that the angle $\Phi(t) = \frac{1}{2}(\phi_1 + \phi_2)$ is then a monotonically increasing or monotonically decreasing function depending on the signs of the invariants E, M_z . The motion of each spin thus consists, in general, of a nonuniform precession about the symmetry axis accompanied by a periodic nutational wiggle with both meridional and azimuthal components.

In general, the time evolution of this system is characterized by two independent frequencies. The first frequency is determined by the period of the functions (III.20) as

$$\tau_1(E, M_z) = 4/aK(z_0/a) = 2\pi/\omega_1(E, M_z) \quad (\text{III.24})$$

where $K(x)$ is a complete elliptic integral, and the second frequency by the secular term in the time integral of the periodic function (III.23):

$$\omega_2(E, M_z) = \frac{1}{\tau_1} \int_0^{\tau_1} dt \dot{\Phi}(t). \quad (\text{III.25})$$

In the following special situations the spin motion is particularly simple: (i) $U = 0$ i.e. $E = \pm(1 - M_z^2)$: The fictitious particle is at rest at $z = 0$ implying that both spins point to the same latitude ($\vartheta_1 = \vartheta_2$) and to the same meridian ($\phi_1 = \phi_2, E < 0$) or to opposite meridians ($\phi_1 = \phi_2 + \pi, E > 0$). The motion of both spins is then a uniform precession according to (III.23) with $z \equiv \zeta \equiv 0$. (ii) $M_z = 0$ i.e. $U = \frac{1}{2}(1 - E^2)$. There is no precessional motion: $\dot{\Phi} \equiv 0$. The combined meridional and azimuthal motion is strictly periodic as opposed to quasiperiodic in the general case. (iii) $E = 0$ i.e. $U = \frac{1}{2}(1 - M_z^2)^2$: The spin motion is purely meridional with $\phi_1 - \phi_2 = \pm\pi/2 = \text{const}$ and $\dot{\Phi} = 0$.

Finally, we might mention the static solutions representing the two types of equilibrium states: (i) spins parallel or antiparallel in the xy -plane ($E = 0, U = 0$); (ii) spins parallel ($E = 0, U = 0$) or antiparallel ($E = 0, M_z = 0$) along the z -axis. In the (z, \dot{z}) phase plane of the meridional motion, the solutions for $E = U = 0$ are represented by an elliptic fixed point at $z = 0$ and the solutions for $E = M_z = 0$ by a pair of hyperbolic fixed points at $z = \pm 1$. The (non-periodic) motion along the separatrix which connects the two hyperbolic fixed points is obtained from (III.20) for $a = z_0 = 1$:

$$z_{\text{sep}}(t) = \pm \tanh(t). \quad (\text{III.26})$$

C. Trajectories for arbitrary γ : invariant tori and fixed points

For general γ , the spin motion of the integrable model \mathbf{H} is considerably more complex except for special initial conditions. The equations of motion for the four angular variables read

$$\begin{aligned} \dot{\vartheta}_1 &= \sin \vartheta_2 [\sin(\phi_1 - \phi_2) + \gamma \sin(\phi_1 + \phi_2)] \\ \dot{\phi}_1 &= \cot \vartheta_1 \sin \vartheta_2 [\cos(\phi_1 - \phi_2) \\ &\quad + \gamma \cos(\phi_1 + \phi_2)] \end{aligned} \quad (\text{III.27})$$

and $1 \leftrightarrow 2$, and the two integrals of the motion are

$$E = -\sin \vartheta_1 \sin \vartheta_2 [\cos(\phi_1 - \phi_2) + \gamma \cos(\phi_1 + \phi_2)] = \text{const} \quad (\text{III.28})$$

$$\begin{aligned} I &= (1 + \gamma^2)(\sin^2 \vartheta_1 + \sin^2 \vartheta_2) \\ &\quad - 2(1 - \gamma^2) \cos \vartheta_1 \cos \vartheta_2 \\ &\quad + 2\gamma(\sin^2 \vartheta_1 \cos 2\phi_1 + \sin^2 \vartheta_2 \cos 2\phi_2) = \text{const}. \end{aligned} \quad (\text{III.29})$$

The increase in complexity is obviously related to the fact that the second invariant, I , can no longer be used to disentangle the meridional and the azimuthal motion as in the limit $\gamma = 0$ [11]. Since the model H_γ is integrable, all trajectories in the 4D phase manifold $(\vartheta_1, \vartheta_2, \phi_1, \phi_2)$ are confined to 2D invariant tori. Any particular 2D invariant torus is obtained geometrically as the intersection in 4D phase space of two 3D hypersurfaces $E = \text{const}$ and $I = \text{const}$ corresponding to particular values of the two integrals of the motion (III.28) and (III.29). On the surface of section defined by $\vartheta_2 = \pi/2$, which we shall use throughout this paper, the two analytic invariants E and I are represented by 2D surfaces and the invariant tori by 1D objects (lines).

The existence of the two analytic invariants E and I implies that the entire 3D reduced space $(\vartheta_1, \phi_1, \phi_2)$ corresponding to the Poincaré cut hyperplane $\vartheta_2 = \pi/2$ is foliated by two sets of smooth surfaces. The fact that the Poincaré cut of any trajectory is confined to the intersection of two such smooth surfaces, which always results in a set of smooth lines or a finite set of isolated points, imposes a severe limitation on its degree of complexity. This is in contrast to the nonintegrable model to be discussed in Sect. IV, where $E = \text{const}$ is the only set of smooth surfaces in $(\vartheta_1, \phi_1, \phi_2)$ -space.

In the following, we study the question how the set of phase-space trajectories changes its character as the anisotropy parameter is varied between the two limits $\gamma = 0$ and $\gamma = 1$ discussed previously. For an optimal perspective of the phenomena of interest, we study selected trajectories specified by the following two types of initial conditions:

- (i) $\vartheta_1^{(0)} = \vartheta_2^{(0)} = \pi/2, \quad -\pi/2 \leq \phi_1^{(0)} \leq \pi/2.$
- (ii) $\vartheta_2^{(0)} = \pi/2, \quad \phi_1^{(0)} = -\pi/4, \quad 0 \leq \vartheta_1^{(0)} \leq \pi/2.$

The fourth angle, $\phi_2^{(0)}$, is determined [12] by the value of the energy, in this case $E = -0.09957501$. In Fig. 3 we present a series of graphs representing the projection

onto the (ϑ_1, ϕ_1) -plane of the Poincaré surface of section ($\vartheta_2 = \pi/2, \dot{\vartheta}_2 > 0$) of a number of such trajectories.

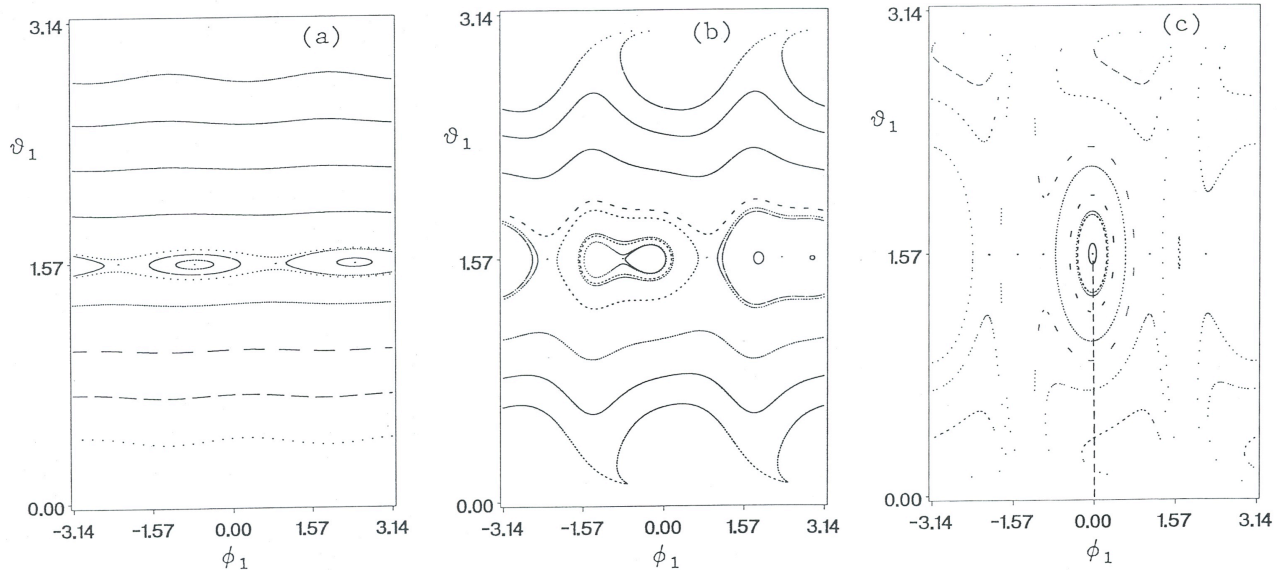


FIG. 3: Three sets of phase-space trajectories for the integrable classical 2-spin model H_γ with (a) $\gamma = 0.01$, (b) $\gamma = 0.1$ and (c) $\gamma = 0.5$, all for the same energy $E = -0.09957501$ and with initial conditions as specified in the text. The graph of each trajectory results from an integration over a time interval of length $\Delta t = 2000$. Each one of the three plots shows the projection onto the (ϑ_1, ϕ_1) -plane of the Poincaré surface of section ($\vartheta_2 = \pi/2, \dot{\vartheta}_2 > 0$) of the tori. For all the trajectories represented in Fig. 3, the alternative Poincaré surface of section ($\vartheta_2 = \pi/2, \dot{\vartheta}_2 < 0$) shows exactly the same pattern but reflected at the axis $\phi_1 = 0$. The dashed line in (c) specifies a line of initial conditions for which time averages of a dynamical variable over single trajectories are presented in Fig. 6 (see discussion in Sect. V).

Figure 3(a) shows a set of trajectories for the case of very weak exchange anisotropy: $\gamma = 0.01$. We observe a pattern which is typical for integrable models: two sets of closed curves (cuts through tori) winding around elliptic fixed points, confined by a separatrix (not shown) which connects a pair of hyperbolic fixed points. Curves with a different topology are found on the other side of the separatrix. As γ approaches zero, the regions with the closed curves shrink and ultimately disappear. For $\gamma = 0$, this particular cut through the tori leads to a set of straight horizontal lines as a result of the conservation law $\cos \vartheta_1 + \cos \vartheta_2 = \text{const}$. In Fig. 3(b), which shows the corresponding picture for a somewhat stronger exchange anisotropy ($\gamma = 0.1$), we notice that what appeared to be a single elliptic fixed point [in Fig. 3(a)] is actually a pair of elliptic fixed points with a hyperbolic fixed point in between. This hyperbolic fixed point is part of another separatrix which separates curves winding around one elliptic fixed point from curves winding around both. Further increase of the exchange anisotropy results in a distortion of the existing pattern with the curves winding

around one of the secondary elliptic fixed points becoming more and more dominant [see Fig. 3(c)] until (in the limit $\gamma = 1$ discussed in Sect. III.1) no other types of trajectories are left.

The equations of motion of H_γ (or, in fact, of the more general model (II.5)) are invariant under a symmetry group generated by the twofold rotations $C_2^{x,y,z}$ about the coordinate axes, the inversion I in spin space combined with time reversal, and the permutation P of the two particles. Whereas the Poincaré hyperplane $\vartheta_2 = \pi/2$ is invariant under all transformations not involving a particle permutation, the direction of any trajectory through this plane is left invariant only by two transformations:

$$\begin{aligned} \text{(a) } C_2^z &: (S_l^x, S_l^y, S_l^z) \rightarrow (-S_l^x, -S_l^y, S_l^z) \\ &(\vartheta_l, \phi_l) \rightarrow (\vartheta_l, \phi_l \pm \pi) \\ \text{(b) } IC_2^z &: (S_l^x, S_l^y, S_l^z) \rightarrow (S_l^x, S_l^y, -S_l^z) \\ &(\vartheta_l, \phi_l) \rightarrow (\pi - \vartheta_l, \phi_l) \end{aligned}$$

combined with time reversal.

The Poincaré cut of any trajectory then either has the

symmetries (a) and (b) or is transformed into the cut of a symmetry-equivalent trajectory. These general symmetry properties are clearly reflected in Fig. 3.

The fixed points in the Poincaré surface of section represent special kinds of periodic phase-space trajectories. Further periodic trajectories can be found in abundance on rational tori, which are dense in phase space. Most of them disappear if the model is subjected to a nonintegrable perturbation. It is interesting that some of these fixed-point periodic trajectories can be analyzed exactly, in fact not only for the integrable model H_γ but also for its nonintegrable counterpart H_α to be discussed in Sect. IV. This is due to the fact that any submanifold of the phase space consisting of all points which are invariant under some subgroup of the symmetry group is invariant under the time evolution of the system. For the models H_γ and H_α , there exist four such submanifolds of dimension 2:

- (i) PC_2^x : $S_1^x = S_2^x$, $S_1^y = -S_2^y$, $S_1^z = -S_2^z$
 $\rightarrow \vartheta_1 = \pi - \vartheta_2$, $\phi_1 = -\phi_2$
- (ii) PC_2^y : $S_1^x = -S_2^x$, $S_1^y = S_2^y$, $S_1^z = -S_2^z$
 $\rightarrow \vartheta_1 = \pi - \vartheta_2$, $\phi_1 = \pi - \phi_2$
- (iii) PC_2^z : $S_1^x = -S_2^x$, $S_1^y = -S_2^y$, $S_1^z = S_2^z$
 $\rightarrow \vartheta_1 = \vartheta_2$, $\phi_1 = \phi_2 + \pi$
- (iv) P : $S_1^x = S_2^x$, $S_1^y = -S_2^y$, $S_1^z = S_2^z$
 $\rightarrow \vartheta_1 = \vartheta_2$, $\phi_1 = \phi_2$.

All trajectories confined to one of these submanifolds represent the time evolution of a dynamical system with only one degree of freedom, and the equations of motion (III.27) can be solved explicitly. The dynamical problem again reduces to that of the bounded motion of a fictitious particle of unit mass in a 1D quartic potential, and the most general solution is expressible in terms of Jacobi elliptic functions. The two types of hyperbolic fixed points in Fig. 3(b) correspond to periodic trajectories of this kind with symmetries PC_2^x and PC_2^y , respectively [13].

IV. THE XY MODEL WITH SINGLE-SITE ANISOTROPY: A NONINTEGRABLE MODEL

In this section we study the dynamical properties of another XY-type 2-spin model, the XY model with single-site anisotropy, described by the Hamiltonian

$$H_\alpha = - (S_1^x S_2^x + S_1^y S_2^y) - \frac{1}{2} \alpha [(S_1^x)^2 - (S_1^y)^2 + (S_2^x)^2 - (S_2^y)^2], \quad (\text{IV.1})$$

The equations of motion (II.1) for H_α read

$$\begin{aligned} \dot{S}_1^x &= -S_1^z S_2^y + \alpha S_1^y S_1^z \\ \dot{S}_1^y &= S_1^z S_2^x + \alpha S_1^x S_1^z \\ \dot{S}_1^z &= S_1^x S_2^y - S_1^y S_2^x - 2\alpha S_1^x S_1^y \end{aligned} \quad (\text{IV.2})$$

and $1 \leftrightarrow 2$. In contrast to H_γ , the model with exchange anisotropy discussed in Sect. III, H_α is, in general, nonintegrable. In particular, the criterion (II.6) for the existence of a second integral of the motion is only satisfied either for $\alpha = 0$, which is identical to the case $\gamma = 0$ of H_γ discussed in Sect. III.B, or for $\alpha = \pm 1$. The integrability of $H_{\alpha=\pm 1}$ is not obvious from the point of view of simple symmetry considerations. The second integral of the motion, which guarantees integrability in the two limits, is

$$M_z = \frac{1}{2}(S_1^z + S_2^z) = \text{const} \quad (\alpha = 0) \quad (\text{IV.3})$$

$$I = -S_1^x S_2^x + S_1^y S_2^y + S_1^z S_2^z = \text{const} \quad (\alpha = 1) \quad (\text{IV.4})$$

A. Trajectories for $\alpha = 1$: an effective one-spin model

The time evolution of the integrable 2-spin model $H_{\alpha=1}$ can be mapped onto that of an effective (autonomous) 1-spin model. In terms of the new variables

$$\begin{aligned} \sigma_x &\equiv S_1^x + S_2^x, & \sigma_y &\equiv S_1^y - S_2^y, & \sigma_z &\equiv S_1^z - S_2^z \\ \tau_x &\equiv S_1^x - S_2^x, & \tau_y &\equiv S_1^y + S_2^y, & \tau_z &\equiv S_1^z + S_2^z \end{aligned} \quad (\text{IV.5})$$

the two integrals of the motion (IV.1) and IV.4) read

$$E = -\frac{1}{2}\sigma_x^2 + \frac{1}{2}\sigma_y^2 = \text{const} \quad (\text{IV.6})$$

$$2(1 - I) = \sigma_x^2 + \sigma_y^2 + \sigma_z^2 = \text{const}. \quad (\text{IV.7})$$

Hamiltonian $H_{\alpha=1}$ describes an effective one-spin system: the spin \mathbf{a} has length $\sqrt{2(1 - I)}$ and satisfies the equations of motion

$$\dot{\sigma}_x = \sigma_y \sigma_z, \quad \dot{\sigma}_y = \sigma_x \sigma_z, \quad \dot{\sigma}_z = -2\sigma_x \sigma_y \quad (\text{IV.8})$$

which are integrable since the Hamiltonian does not depend explicitly on time. Once the solution $\sigma(t)$ of (IV.8) has been determined, the equations of motion for the τ_μ ,

$$\dot{\tau}_x = \sigma_y \tau_z, \quad \dot{\tau}_y = \sigma_x \tau_z, \quad \dot{\tau}_z = -\sigma_y \tau_x - \sigma_x \tau_y \quad (\text{IV.9})$$

describe the motion of a spin τ in a time-dependent external field $\mathbf{h}(t) = (\sigma_x(t), \sigma_y(t), 0)$. The solution of Eqs. (IV.8) is readily obtained in terms of angular coordinates ϑ, ϕ defined by

$$(\sigma_x, \sigma_y, \sigma_z) = \sqrt{2(1 - I)} (\sin \vartheta \cos \phi, \sin \vartheta \sin \phi, \cos \vartheta) \quad (\text{IV.10})$$

again by mapping the effective 1-spin problem onto that of a fictitious particle of unit mass in a quartic potential $V(u)$:

$$\frac{1}{2} \dot{u}^2 + V(u) = E^2 / (I - 1) = \text{const} \quad (\text{IV.11})$$

with

$$V(u) = -(1 - I)(1 - u^2)^2 \quad (\text{IV.12})$$

where

$$u = \cos \vartheta, \quad v = \frac{-\dot{u}}{\sqrt{2(1-I)(1-u^2)}} = \sin 2\phi. \quad (\text{IV.13})$$

Again the solutions are periodic Jacobi elliptic functions. The second independent fundamental frequency in this integrable 2-spin model $H_{\alpha=1}$ makes its appearance in the solution of the linear differential Eqs. (IV.9) with time-dependent coefficients given by the solutions of (IV.8).

B. Trajectories for arbitrary α : fixed points, tori and chaos

As has already been pointed out, the two models H_γ and H_α , which are identical for $\alpha = \gamma = 0$, have the same symmetry for nonzero α , and for $\gamma \neq 0, \pm 1$. In Sect. III.3 we have studied the Poincaré surface of section ($\vartheta = \pi/2, \dot{\vartheta}_2 > 0$) of selected trajectories as they change with increasing exchange anisotropy, which constitutes an integrable perturbation of the rotational symmetry (see Fig. 3). It is, therefore, most interesting to investigate how a corresponding set of trajectories changes with increasing single-site anisotropy, which constitutes a nonintegrable perturbation with the same symmetry.

For very weak single-site anisotropy, for example $\alpha = 0.01$, we obtain a picture which is virtually indistinguishable from Fig. 3(a) representing the case of a very weak exchange anisotropy ($\gamma = 0.01$). Qualitative differences such as the presence of chaotic trajectories in H_α or differences in the pattern of fixed points become visible only on considerably smaller scales. However, already for $\alpha = 0.1$ and $\gamma = 0.1$, the differences between the trajectories of the two models become quite prominent [compare Figs. 4(a) and 3(b)]. In particular, there are only two pairs of fixed points on the line $\vartheta = \pi/2$ in the nonintegrable case: one pair of elliptic fixed points and one pair of hyperbolic ones. Again one can determine analytically four classes of periodic trajectories corresponding to the symmetries (i)-(iv) discussed in Sect. III.3. As in the model H_γ , these periodic solutions can be expressed in terms of Jacobi elliptic functions [14]. The two hyperbolic fixed points are connected by a relatively narrow chaotic ‘separatrix’. No further chaotic regions are visible on this scale.

As we move further away from the integrable limit $\alpha = 0$ by increasing the value of the anisotropy parameter to $\alpha = 0.5$, chaos becomes more widespread in phase space [see Fig. 4(b)]. We now observe a broad band of chaos around the primary elliptic fixed points of symmetry (i) and connecting the (primary) hyperbolic fixed points of symmetry (ii). Outside of it, regular trajectories stay predominant. The destruction of the rational tori about the primary elliptic fixed points now features prominently. One such rational torus has left behind two pairs of closed trajectories with period 2 in the cut and with tori winding around them. These secondary elliptic

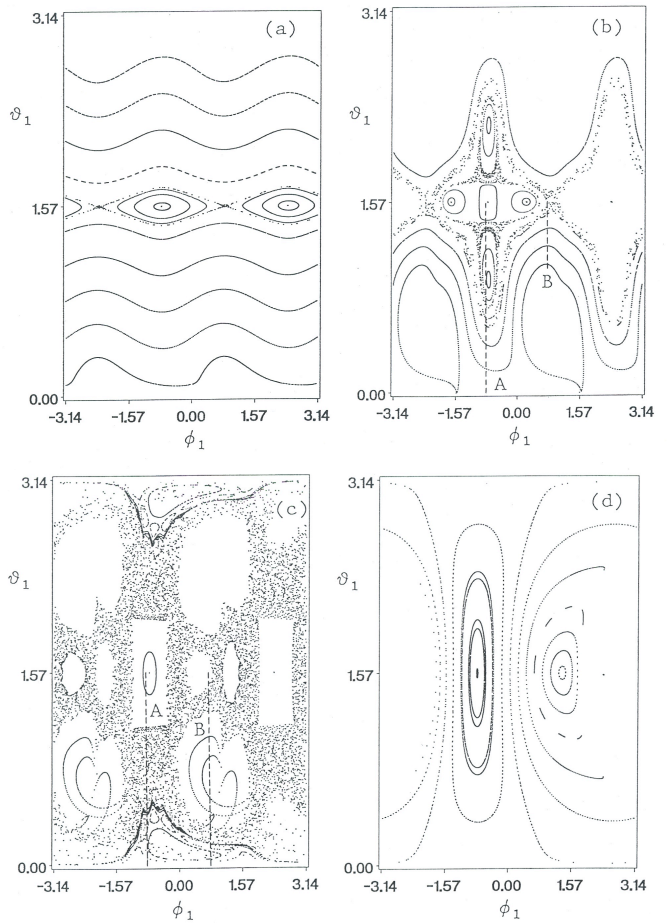


FIG. 4: Four sets of phase-space trajectories for the classical 2-spin model H_α with (a) $\alpha = 0.1$, (b) $\alpha = 0.5$, (c) $\alpha = 0.7$ and (d) $\alpha = 1.0$, all for the same energy $E = -0.09957501$ and with initial conditions as specified in the text (see Sect. III.3). The graphs of these trajectories result from integrations over time intervals of length up to $\Delta t = 5000$ ($\Delta t = 25000$ in one particular case, the chaotic itinerary which dominates (c)). Each one of the four plots shows the projection onto the (ϑ_1, ϕ_1) -plane of the Poincaré surface of section ($\vartheta = \pi/2, \dot{\vartheta}_2 > 0$) of the (regular and chaotic) trajectories. The dashed lines in (b) and (c) specify lines of initial conditions for which time averages of a dynamical variable over single trajectories (itineraries) are presented in Figs. 7 and 8 (see discussion in Sect. V).

fixed points (in the cut) are accompanied by an equal number of hyperbolic ones and surrounded by bands of chaos. It is important to note that this second chaotic region, which is most prominent in the vicinity of the four secondary hyperbolic fixed points and encircles the four regular islands centered by the secondary elliptic fixed points, is no longer separated by any intact torus from the broad chaotic band. However, the phase flow between the two chaotic regions is strongly obstructed by the presence of at least two low-flux cantori [15]. Further cantori

separate this chaotic region from chaotic regions which envelop just two of the four regular islands about the secondary elliptic fixed points as will be discussed further in connection with Fig. 9 in Sect. V. We thus have one large chaotic region bounded by the meandering curves on the outside, and compartmentalized by different sets of cantori.

The picture changes dramatically as we increase the amount of single-site anisotropy to $\alpha = 0.7$ [see Fig. 4(c)]. Most of the invariant tori which are still present for $\alpha = 0.5$ have now evaporated and are replaced by a wide sea of chaos interspersed with small islands of tori winding tightly around certain periodic trajectories. While chaos has increased substantially on a global basis between $\alpha = 0.5$ and $\alpha = 0.7$, it begins to give way to intact tori in the vicinity of the elliptic fixed point (at $\vartheta_1 = \pi/2$, $\phi_1 \simeq -0.756$) even before reaches the value of 0.7. More and more tori are restored until, in the integrable limit $\alpha = 1$, shown in Fig. 4(d), a new complete foliation of the phase manifold emerges.

Hence, as the single-site anisotropy parameter increases from $\alpha = 0$ to $\alpha = 1$, one complete foliation of the phase manifold by invariant tori melts away into a sea of chaos, out of which a new foliation crystallizes, incorporating only small fragments of the old foliation in its own structure. This is contrasted by the model H_γ , in which the two foliations for $\gamma = 0$ and $\gamma = 1$, respectively, are connected by a sequence of complete foliations.

C. The elusiveness of chaotic trajectories

Before we proceed with the analysis of the geometric structure of invariants in the nonintegrable 2-spin model H_α , we have to comment on the two types of trajectories which are present: regular trajectories and chaotic trajectories. Regular trajectories are confined to 2D surfaces (invariant tori) in 4D phase space, and are characterized by not more than 2 fundamental frequencies. Each 2D invariant torus divides the 3D energy hypersurface on which it is located into 2 disconnected parts. Regular trajectories are insensitive to small changes in initial conditions [16]. The inevitable inaccuracy of the numerical integration propagates only very slowly, so slowly that the trajectory can be determined with confidence for time intervals which are sufficiently long for the determination of any physical property of interest. For regular trajectories there is no alternative to winding perpetually around invariant tori in a regular pattern.

In the nonintegrable model H_α where the population of primary invariant tori is nowhere dense in phase space, the tori act as impenetrable limits to the range of chaotic trajectories. Chaotic trajectories are still strictly confined to move on a single 3D energy hypersurface; but within a given connected region between intact tori on that hypersurface, their course is seemingly very erratic, lacking any orderly pattern. In contrast to regular trajectories, analytic solutions for chaotic trajectories are out of

reach. Any quantitative description of chaotic trajectories has to rely, therefore, on the numerical integration of the equations of motion. However, the practical numerical integration of a trajectory, be it regular or chaotic, always operates with a finite accuracy. For one thing, the initial conditions are specified only to within a finite accuracy [17]. Consequently, the computation does not discriminate between individual trajectories which originate in the same phase-space volume element Ω_0 . If we disregard the unavoidable additional errors introduced at each step of the integration, the error propagation can be estimated by the growth of the largest diameter $\Delta(t)$ of the phase-space volume element $\Omega(t)$ which originates from Ω_0 at $t = 0$. The rate of growth of Δ is qualitatively different for regular and chaotic trajectories.

In an integrable model or in a phase-space region of a nonintegrable model where invariant tori predominate, $\Delta(t)$ grows (roughly) linearly in time. By contrast, the course of chaotic trajectories is extremely sensitive to slight changes in initial conditions. A characteristic signature of this sensitivity is that the largest diameter of the phase-space volume element Ω_0 , which is a measure of the uncertainty in initial conditions, grows exponentially in time initially, and ultimately fills the entire region between intact tori to which the chaotic trajectories originating in Ω_0 have access.

It is important to point out that this exponential propagation of error and uncertainty occurs only tangentially to any existing analytic invariant in phase space (the energy in the case of H_α). Nevertheless, the determination of any single chaotic trajectory of the dynamical system requires a careful consideration of the rapid error propagation within a given energy hypersurface. In fact, the very notion of a “single chaotic trajectory” loses its meaning in all contexts where one is forced to operate with finite accuracy, which is the case in all numerical calculations and in all applications to physical systems.

Chaotic trajectories are thus extremely elusive to any attempt, however elaborate, of numerical determination. This calls for an answer to the following important question: To what extent does this elusiveness of chaotic trajectories affect numerical studies of various physical properties of nonintegrable dynamical models, particularly quantities which are based on the numerical determination of time averages? It is not a priori clear that such numerical studies invariably lead to meaningful results. In the following, we describe an attempt to cope with this problem in praxis.

D. Itineraries

The classical 2-spin models studied in this paper have two characteristic properties which facilitate the numerical analysis of phase-space trajectories enormously: (i) the equations of motion (II.1) are free of singularities; (ii) both the spin variables themselves, and their time derivatives are bounded from above and below.

For simplicity, we use a 4th order Runge-Kutta method, with fixed time step dr , $RK4[dt]$, to integrate numerically the equations of motion (IV.2) of the 2-spin model H_α . For given initial conditions, this always results in a well-defined time series for arbitrarily long time intervals. Let us call this time series an *itinerary*.

If the initial conditions specify a regular trajectory, then the itinerary is, in general, a very good approximant of that regular trajectory, provided that the time step dt is chosen reasonably small. In fact, the deviation of the itinerary from the trajectory is proportional to the length of the time interval over which the itinerary is evaluated, with a coefficient which can be made very small with little effort. This makes it possible to compute a very close approximant of the regular trajectory for time intervals which are sufficiently long for a precise determination of time averages. If, on the other hand, the initial conditions specify a chaotic trajectory, the itinerary is prone to deviate from that trajectory by a large amount within a relatively short time interval no matter how much we optimize the accuracy of the numerical integration procedure. This is due to the unavoidable exponential error propagation mentioned previously.

For an illustration of this point, we evaluate the time evolution of a chaotic itinerary of H_α a by means of $RK4[dt_1]$. Simultaneously, we determine another itinerary by using the same initial conditions but integrate with $RK4[dt_2 = 2dt_1]$. Naturally, in the limit $dt_1 \rightarrow 0$ [18], which is unrealistic for all practical purposes, the two itineraries converge towards each other and towards the chaotic trajectory over a time interval of increasing length. However, for finite dt_1 , no matter how small, the two itineraries separate from each other within a relatively short time interval, and it is reasonable to assume that the observed rate of divergence is a good indicator for the rate of divergence of the itineraries from the true trajectory. Since the phase manifold of our two-spin system is compact, the two itineraries cannot diverge indefinitely. We therefore terminate the itinerary 2 as soon as its separation from itinerary 1 reaches the value 0.1. We then start a new $RK4[dt_2]$ integration using the instantaneous coordinates of the $RK4[dt_1]$ integration as initial conditions and thus reset the separation to zero (with finite accuracy). The result of this computation is plotted in Fig. 5, which shows on a logarithmic scale the distance between itinerary 1 and a sequence of itineraries 2.

We observe that the separation between neighboring itineraries is, on the average, clearly exponential in character. However, deviations from the exponential behavior occur over time intervals of various sizes including very long ones. They typically manifest themselves in the form of a strongly suppressed rate of separation, occasionally in a decrease of distance. This effect is attributable mostly to the presence of “bottle-necks” in the phase-space region traversed by the chaotic itinerary. In Sect. V we shall discuss the role of these bottle-necks, which have made their imprint on chaotic trajectories

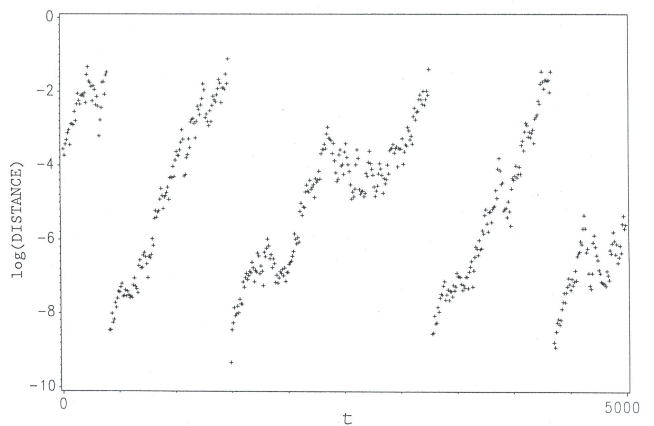


FIG. 5: Logarithm of the distance $[(\mathbf{S}_1^{(2)} - \mathbf{S}_1^{(1)})^2 + (\mathbf{S}_2^{(2)} - \mathbf{S}_2^{(1)})^2]^{1/2}$ in 4D phase space between a chaotic itinerary evaluated with $RK4[dt_1 = 0.005]$ and a sequence of chaotic itineraries evaluated by using $RK4[dt_2 = 2dt_1]$ as a function of time over a time interval of length $\Delta t = 5000$. The calculation uses 16 significant digits. The two itineraries start out with the same initial conditions. Whenever the distance reaches the value 0.1, itinerary 2 is terminated and replaced by a new itinerary using again $RK4[dt_2]$ and the instantaneous coordinates of itinerary 1 as initial conditions. The time interval between successive data points is 10. The present result is for $H_{\alpha=0.5}$ and the following initial conditions: $\vartheta_1^{(0)} = 2.4484$, $\vartheta_2^{(0)} = 0.7702$, $\phi_1^{(0)} = -3.1330$, $\phi_2^{(0)} = -1.8026$.

even on the largest time scales analyzed in our calculations ($t \sim 10^6$). Specifically, they are responsible for the occurrence of long-time anomalies which slow down the convergence of time averages immensely.

The chaotic itineraries generated by $RK4[dt]$ reproduce two crucial characteristics of true chaotic trajectories.

- (i) The exponential error propagation does not affect the conservation of any existing analytic invariant of the phase flow. In the case of the two-spin model H_α , the error propagation in the energy can be made very small by a reasonable choice of dt in $RK4[dt]$, irrespective of whether the itinerary is regular or chaotic.
- (ii) The constraints in the form of impenetrable walls imposed by the presence of invariant tori on a given energy hypersurface are respected by chaotic itineraries no less than is expected of true chaotic trajectories [19].

On the other hand, we know that the exact course of a chaotic itinerary is extremely sensitive to the integration procedure (for example, small change of dt in $RK4[dt]$), which is a reflection of the extreme sensitivity of true chaotic trajectories to small changes in initial conditions. To what extent then, one is compelled to ask, can one derive from chaotic itineraries dynamical properties which

are intrinsic properties of the classical 2-spin model in its original definition? To answer this question, we note that even though a small change of dt in $RK4[dt]$ causes an uncontrollably large effect on the exact course of a chaotic itinerary, it does not seem to have any observable effect on its range in a given connected region marked off by intact tori on the energy hypersurface. This suggests that time averages of dynamical variables over chaotic trajectories might, in fact, be well approximated by time averages over the corresponding chaotic itineraries. In the following we report the results of a numerical study of such time averages, which has led to a number of interesting conclusions.

V. TIME AVERAGES: ANALYTIC AND NONANALYTIC INVARIANTS

In autonomous Hamiltonian systems with 2 degrees of freedom, integrability depends on the existence of one analytic invariant which is independent of the Hamiltonian. For the general 2-spin model (II.5), this second integral of the motion exists only if the model parameters satisfy the conditions discussed in Sect. II. On the other hand, invariants can always be constructed numerically, at least in principle: Pick any dynamical variable X which is independent of the Hamiltonian, i.e. which cannot be expressed as a function of H . Then determine the time average of X over the phase-space trajectory specified by the initial condition $(\mathbf{S}_1^{(0)}, \mathbf{S}_2^{(0)})$:

$$\langle X \rangle = \lim_{T \rightarrow \infty} \frac{1}{T} \int_0^T dt X(t, \mathbf{S}_1^{(0)}, \mathbf{S}_2^{(0)}). \quad (\text{V.1})$$

Since the Birkhoff theorem [20] guarantees the existence of the time average (V.1) for almost all initial conditions, this procedure defines a (generalized) function

$$\langle X \rangle = \tilde{I}(\mathbf{S}_1, \mathbf{S}_2) \quad (\text{V.2})$$

everywhere in phase space except for a set of points with measure zero. The integrability of the phase flow governed by H is then associated with the analyticity of the function $\tilde{I}(\mathbf{S}_1, \mathbf{S}_2)$.

A. Integrable model H_γ

Let us first consider the completely integrable model H_γ discussed in Sect. III. The two analytic invariants which guarantee integrability are the energy $E = H_\gamma$ given in (III.1) by definition and the function I given in (III.3) by analytic construction. The function $\tilde{I}(\mathbf{S}_1, \mathbf{S}_2)$ as obtained from time averages (V.1) over all trajectories, which are all regular in this case, is then necessarily some function of E and I . Hence $\tilde{I}(\mathbf{S}_1, \mathbf{S}_2)$ is itself an *analytic invariant*. For an illustration of this point, we present in the following some numerical results of time averages for the integrable model H_γ .

We determine the time averages and estimate the accuracy of our results as follows: We integrate the equations of motion by using $RK4[dt = 0.005]$ and consider the values of the itinerary at intervals $\tau = 0.1$ for $0 < t < 1000$. Let \bar{X} be the average of the dynamical variable X over these 10000 values. Next we determine $\bar{\bar{X}}$, the average over 10 successive values of \bar{X} , and $(\sigma_{\bar{X}})^2$, the mean-square departure of \bar{X} from $\bar{\bar{X}}$. If the value of $\sigma_{\bar{X}}$ is less than $5 \cdot 10^{-5}$, the calculation is terminated, and the time average and its standard deviation is determined as follows:

$$\langle X \rangle = \bar{\bar{X}}, \quad \sigma = \sigma_{\bar{X}} = \left[\frac{1}{10} \sum_{i=1}^{10} (\bar{X}_i - \langle X \rangle)^2 \right]^{1/2}. \quad (\text{V.3})$$

Otherwise we repeat the procedure described above N times by continuing the integration of the itinerary over further intervals of length 10 000. The calculation is terminated if two successive values of $\sigma_{\bar{X}}$ are less than $5 \cdot 10^{-5}$ and the corresponding values \bar{X} differ by less than $5 \cdot 10^{-4}$ or, in the absence of convergence, after $N = 10$ iterations. In this case, the time averages and their standard deviations are determined as follows:

$$\langle X \rangle = \frac{1}{N} \sum_{i=1}^N \bar{\bar{X}}_i, \quad \sigma = \sigma_{\bar{X}} = \left[\frac{1}{N} \sum_{i=1}^N (\bar{X}_i - \langle X \rangle)^2 \right]^{1/2}. \quad (\text{V.4})$$

In (V.3) the time average is over an interval of length 10000, in (V.4) over an interval of N times that size.

In the context of our current discussion, we have evaluated the quantities $\langle (S_1^\mu)^2 \rangle$, $\mu = x, y$ of $H_{\gamma=0.5}$ for a set of initial conditions which are specified by the dashed line in Fig. 3(c). For each one of 98 different sets of initial conditions on that line, we have determined the quantities $\langle (S_1^\mu)^2 \rangle$, $\mu = x, y$. In all cases except one we have found convergence to within 5 parts in 10^4 after $N \leq 3$ iterations. In Fig. 6 we have plotted the quantities $\langle (S_1^\mu)^2 \rangle$, $\mu = x, y$ as functions of ϑ_1 . The data indeed indicate a continuous, piecewise smooth, ϑ_1 -dependence of this analytic invariant. Note the presence of two cusp-like singularities in each quantity. These singularities are associated with separatrices in the phase flow, which mark the boundaries between tori of three different types of topology [see Fig. 3(c)] [21]. The slow convergence of $\langle (S_1^y)^2 \rangle$ for the data point at $\vartheta_1 = 0.7383$ is due to the “critical slowing down” near one of the two separatrices. This critical slowing down near separatrices and a similar phenomenon occurring near rational tori is the only mechanism in integrable models which can give rise to slow convergence in time averages. This type of “long-time anomaly” is of no serious concern and easy to cope with in praxis. Different types of long-time anomalies, which are much more difficult to deal with, occur in non-integrable models.

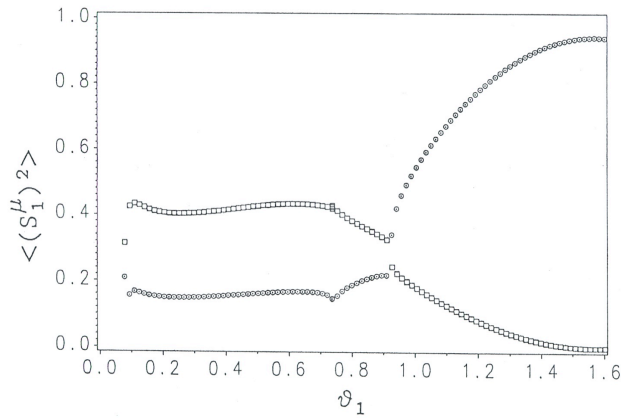


FIG. 6: Time averages $\langle (S_1^x)^\mu \rangle$ (circles) and $\langle (S_1^y)^\mu \rangle$ (squares) over single trajectories of the integrable model $H_{\gamma=0.5}$ as a function of the initial value ϑ_1 for initial conditions specified by the dashed line in Fig. 3(c), which is, in fact, the projection of a curved line on the energy surface $E = -0.09957501$ onto the Poincaré plane of section $\vartheta_2 = \pi/2$. All data points (except for one) represent averages over a time interval of length $T = 10^4$ and an uncertainty of less than 5 parts in 10^4 . The one data point at $\vartheta_1 = 0.7383$ marked by a symbol with a somewhat larger vertical width represents a time average over $T = 10^5$; in this case the uncertainty of the result is indicated by the width of the symbol.

B. Nonintegrable model H_α

We now turn to the analysis of time averages in the nonintegrable model H_α discussed in Sect. IV. For $0 < \alpha < 1$, the energy is the only integral of the motion. The quantity $\tilde{I}(\mathbf{S}_1, \mathbf{S}_2)$ as obtained from the averages (V.1) of a dynamical variable X is no longer an analytic function of the initial conditions even though it is well defined everywhere in phase space except for a set of measure zero. We may call it a *nonanalytic invariant*. The nonanalyticities of $\tilde{I}(\mathbf{S}_1, \mathbf{S}_2)$ are associated with the occurrence of chaotic trajectories. Chaotic trajectories are dense in phase space. Hence $\tilde{I}(\mathbf{S}_1, \mathbf{S}_2)$ is not an (analytic) integral of the motion; nowhere in phase space can it assume the role of an action variable. Note that the nonanalytic nature of $\tilde{I}(\mathbf{S}_1, \mathbf{S}_2)$ can emerge, strictly speaking, only if the averaging in (V.1) is done over an infinite time interval. This underlines the fact that chaos is a long-time asymptotic property of dynamical systems. Nevertheless, the numerical evaluation of time averages (necessarily over finite time intervals) allows us to determine $\tilde{I}(\mathbf{S}_1, \mathbf{S}_2)$ approximately and to study the nature of its nonanalyticities. Before we proceed to discuss our numerical results, let us summarize what one might reasonably expect:

- (i) In regions on the energy hypersurface where regular trajectories prevail, $\tilde{I}(\mathbf{S}_1, \mathbf{S}_2)$ is expected to exhibit a fairly smooth dependence on initial conditions, qualitatively similar to the results for an integrable

model (see Fig. 6).

- (ii) If it is assumed that the phase flow within a connected region of chaos on the energy hypersurface is ergodic, then $\tilde{I}(\mathbf{S}_1, \mathbf{S}_2)$ is constant in this region. Since chaotic trajectories are dense on the energy hypersurface, even the "smooth" parts of $\tilde{I}(\mathbf{S}_1, \mathbf{S}_2)$ in the regular regions would then consist of horizontal portions albeit of very small sizes.
- (iii) At the boundary between a chaotic region and a regular region, the phase-space region sampled by the trajectory changes abruptly. Therefore, we expect a discontinuity in the time average $\tilde{I}(\mathbf{S}_1, \mathbf{S}_2)$. These discontinuities are one manifestation of what we have been calling nonanalyticity.

However, in view of the intricate structure of regular islands and cantori typically present in the border region, we have to anticipate complications not represented in this simplified picture.

In the following we shall focus on time averages $\langle (S_1^y)^\mu \rangle$ of $H_{\alpha=0.5}$ and $H_{\alpha=0.7}$. At first we consider two lines of initial conditions on the same energy hypersurface of $H_{\alpha=0.7}$, illustrated in Fig. 4(c). The Poincaré surface of section is dominated by widespread chaos interspersed by regular islands. The line A of initial conditions starts out (at $\vartheta_1 = \pi/2$) near the center of a regular island, then traverses the wide sea of chaos before it enters (at $\vartheta_1 \simeq 0.4$) a region of regular islands surrounded by chaos which is considerably more confined.

The time averages of $\langle (S_1^y)^\mu \rangle$ for 102 equally spaced initial conditions are shown in Fig. 7(a). We observe that in the regular region in the vicinity of $\vartheta_1 = \pi/2$, the nonanalytic invariant $\tilde{I}(\mathbf{S}_1, \mathbf{S}_2) = \langle (S_1^y)^\mu \rangle$ has a ϑ_1 -dependence which is extremely smooth, very reminiscent of the results found for the integrable model H_γ (see Fig. 6). In the region near the opposite end of line A , chaos is considerably more developed than on the center island. Here, nonanalyticities in $\langle (S_1^y)^\mu \rangle$, in the form of small discontinuities, are indeed observable. Nevertheless, convergence is fairly quick even for the chaotic itineraries. Very much slower convergence is observed, however, for the itineraries which are located in the region of widespread chaos. Almost all data points within that chaotic region are consistent with a constant, which suggests that the phase flow is indeed ergodic within that region. Note, however, that a few of the data points have extra large error bars indicating particularly slow convergence.

We have evidence that this slow convergence is a consequence of an important phenomenon described previously for area-preserving maps [22-24]. In that context, it was observed that the boundaries of chaotic regions tend to appear "sticky" to chaotic trajectories in the following sense: The ultimate wall which constrains the range of a chaotic trajectory must be an intact torus. This outermost torus of a regular island, which has been termed "boundary cycle" [24] must be (according to arguments discussed in [24]) a "critical torus", i.e. a torus which is

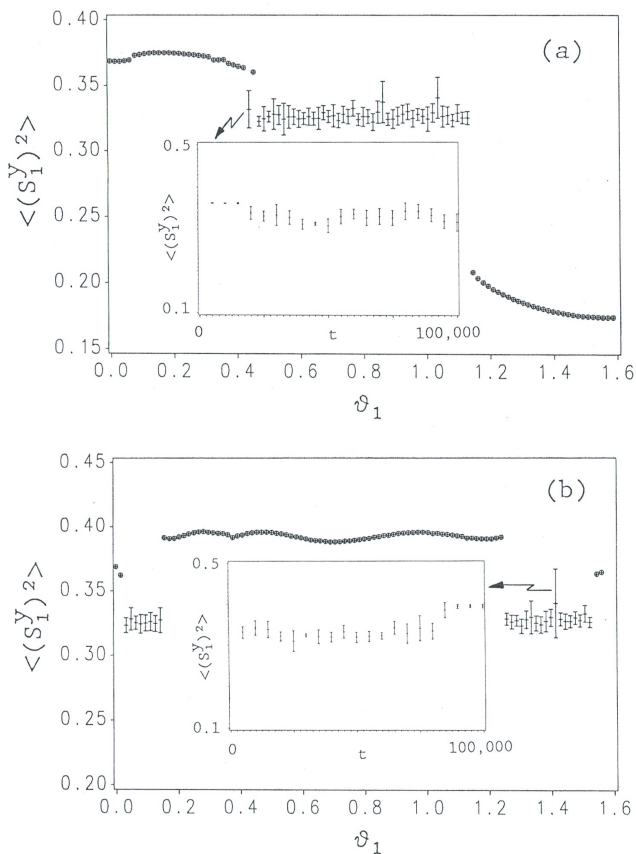


FIG. 7: Time average $\langle (S_1^y)^2 \rangle$ over single itineraries of the nonintegrable model $H_{\alpha=0.7}$ as a function of the initial value ϑ_1 for initial conditions specified (a) by the dashed line *A* and (b) by the dashed line *B* in Fig. 4(c). Circles represent time averages over a time interval $T \leq 3 \cdot 10^4$ which have rapidly converged. The remaining data points represent time averages over a time interval $T = 10^5$ which are subject to long-time anomalies. The error bars denote the standard deviation as defined in (V.4). The insets show sequences of time averages over successive time intervals $\Delta t = 5000$ for two selected itineraries which are particularly strongly affected by long-time anomalies.

exactly at the point of losing its smoothness and at the same time at the point where it starts to degenerate into a Cantor set. Consequently, the boundary cycle is coated on the side towards the chaotic region, by an infinite sequence of cantori which accumulate at the critical torus. Successive cantori are separated by chains of regular islands which are embedded in narrow chaotic bands. Any trajectory which samples the large chaotic region ergodically, will sooner or later penetrate this border layer and get trapped for some period of time in the labyrinth of cantori and island chains, which themselves have their own boundary layers consisting of an infinite sequence of cantori and islet chains, and so on ad infinitum. This is what makes the boundary cycle sticky.

This scenario for nonlinear area-preserving maps holds essentially in its entirety for Poincaré surfaces of section of Hamiltonian systems with 2 degrees of freedom. For one thing, the repeated temporary pause in the exponential separation of chaotic itineraries, which we have observed in the context of our discussion of Fig. 5, can be attributed to precisely this phenomenon. Now let us examine the chaotic itineraries used for the determination of the time averages shown in Fig. 7(a) for the presence of sticky boundaries. We pick out for the purpose of illustration the first data point with an extra large error bar (the point at $\vartheta_1 = 0.4398$). The itinerary which leads to this data point starts out right in the middle of the border area between the regular and the chaotic region. Note that this data point is located between two data points which have converged rapidly. Examination of the itineraries shows that the data point to the left belongs to a cantorus and the data point to the right to a chain of regular islands. The itinerary belonging to the data point in between (the one with a large error bar) thus starts out being trapped in a narrow layer between two cantori during a fairly long time interval (between $t = 0$ and $t_E = 15000$) before it escapes into the large chaotic region. While it sticks to the boundary region, the time average of $\langle (S_1^y)^2 \rangle$ converges fairly rapidly, not unlike the time average over a regular trajectory. This can be seen in the inset to Fig. 7(a), which shows time averages $\langle (S_1^y)^2 \rangle$ over successive intervals of length $\Delta t = 5000$ for that particular itinerary. Once this itinerary has escaped into the chaotic sea, the data points in the inset tend to converge to a different value, but much more slowly so. This thus explains the large error bar in the original data point which represents an average over $\Delta t = 100000$ encompassing both the motion in the boundary region and the motion in the chaotic sea. Evidently, calculations over substantially larger time intervals are needed in order to average out these occasional and temporary confinements. There are two other data points in Fig. 7(a) whose error bars are extra large. These data points belong to itineraries which start out in the chaotic sea and then get trapped in the same boundary layer for a relatively long period of time before they escape back into the sea. It is interesting to note that the other boundary cycle, the one around the center island, is much less sticky.

Similar observations can be made on time averages $\langle (S_1^y)^2 \rangle$ for a different set of initial conditions: line *B* in Fig. 4(c), which cuts across a regular island from one part to another part of the same chaotic sea. The results are shown in Fig. 7(b). Again we find very rapid convergence in the regular region resulting in a piecewise smooth curve in accordance with our expectations. Again the data points resulting from itineraries which sample the chaotic sea are consistent with ergodic flow in that region. Again some data points have particularly large error bars, which are caused by the long time scales induced by the stickiness of the boundary region [see inset to Fig. 7(b)].

In summary, we have numerical evidence that the phase flow in the chaotic sea is ergodic; but the stickiness of the boundary layers gives rise to dynamic patterns with arbitrarily long time scales, which slow down the convergence of time averages considerably. In the context of the studies of area-preserving maps, these long-time anomalies were found to be responsible to a large extent for the slow power-law decay of time-dependent correlation functions [23, 24].

A note of caution is in order. Strictly speaking we have evidence of ergodicity only for itineraries, but not for true chaotic trajectories. However, the fact that the results of our calculations appear to be quite insensitive to various changes in the integration procedure is clearly in support of the conclusion that this ergodicity property applies to true chaotic trajectories as well.

Now we turn to the case $\alpha = 0.5$, where the chaotic regions are considerably more constrained than in the previous case ($\alpha = 0.7$). Let us again discuss the time average $\langle (S_1^y)^2 \rangle$ for two lines of initial conditions A and B on the same energy hypersurface, illustrated in Fig. 4(b). Line A starts out (at $\vartheta_1 = 0$) in a regular region, then cuts through a band of chaos, traverses a regular island which is centered (in the cut) by a secondary elliptic fixed point, then cuts through a narrower band of chaos and, finally, enters the regular island centered by the primary elliptic fixed point. The time average $\langle (S_1^y)^2 \rangle$ for a set of equally spaced initial conditions is shown in Fig. 8(a). Again we observe that the convergence is very rapid in the regular regions, and the ϑ_1 -dependence of the nonanalytic invariant is fairly smooth. So far the results look not unlike those for $\alpha = 0.7$. However, in the chaotic bands we find that the long-time anomalies are much more pronounced, leading to considerably larger error bars. In fact, the data points are now scattered to such an extent that no conclusions about ergodicity can safely be drawn. The same is true for time averages along line B of initial conditions, which are displayed in Fig. 8(b). Line B starts out in the same regular region as line A [see Fig. 4(b)] and enters the same chaotic band, but at a different value of ϕ_1 . It terminates near the primary hyperbolic fixed point.

Our analysis of the long-time anomalies which cause the extremely slow convergence in the chaotic regions reveals the following: The sticky boundary cycles are still present and indeed contribute to the long-time anomalies by trapping chaotic trajectories occasionally and temporarily. However, in this case the dominant mechanism seems to be of a different kind. As we have already pointed out in the context of our discussion of Fig. 4(b), the two main chaotic regions traversed by line A are, in fact, no longer separated by intact tori. The only separation is a series of cantori some of which have low-flux character. Empirically we find that the switching of chaotic itineraries between different large scale chaotic regions is a process which requires much longer times to average out than the occasional trapping in the sticky boundary region. In our case this mechanism defeats any

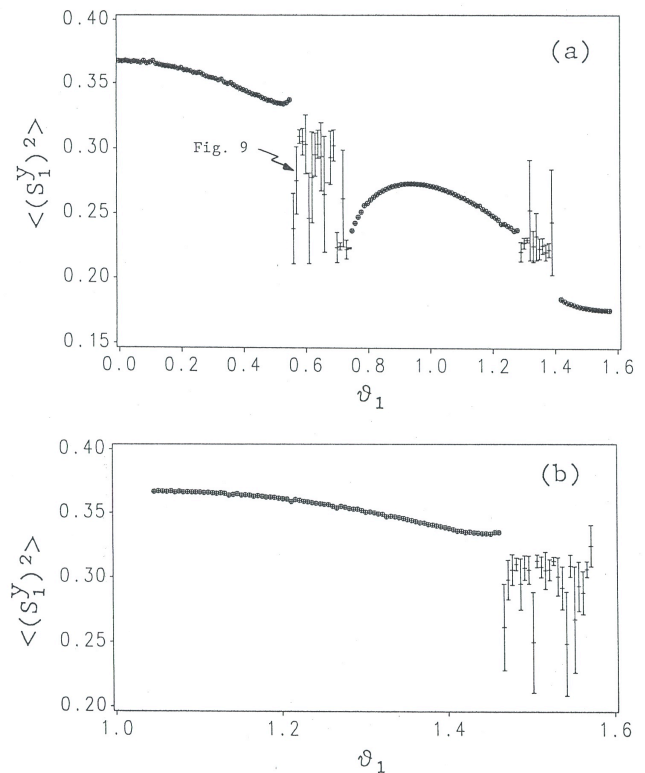


FIG. 8: Time average $\langle (S_1^y)^2 \rangle$ over single itineraries of the nonintegrable model $H_{\alpha=0.5}$ as a function of the initial value ϑ_1 for initial conditions specified (a) by the dashed line A and (b) by the dashed line B in Fig. 4(b). The circles represent time averages over a time interval $T \leq 3 \cdot 10^4$ which have rapidly converged. The remaining data points represent time averages over a time interval $T = 10^5$ which are subject to long-time anomalies. The error bars denote the standard deviation σ defined in (V.4).

reasonable effort to determine time averages with moderate accuracy.

For an illustration of this mechanism, we show in Fig. 9 the Poincaré cuts of a chaotic itinerary for three successive time intervals. The itinerary starts out in the broad band of chaos which connects the two primary hyperbolic fixed points [see Fig. 9(a)]. At time $t_1 \simeq 20000$ the itinerary leaks through a low-flux cantorus into a more localized chaotic band [see Fig. 9(b)], and stays there up to time $t_2 \simeq 40000$ when it crosses another low-flux cantorus to enter a third chaotic region which wraps around the five main regular islands individually [see Fig. 9(c)]. This particular itinerary then stays in that region up to $t = 100000$. Fig. 9(d) shows time averages of $\langle (S_1^y)^2 \rangle$ over successive time intervals of length $\Delta t = 5000$. The systematic change of the mean value at t_1 and t_2 is clearly visible. Note that the convergence is fairly good as long as the itinerary does not cross any of the low-flux cantori, but the convergence of the overall average (marked by an arrow in Fig. 8(a)) is very poor. It is important to real-

ize that these long-time anomalies do not show up in all (nonconserved) dynamical variables. In computing the results for $\langle (S_1^y)^2 \rangle$ shown in Fig. 8, for example, we have

also evaluated the time averages $\langle (S_1^y)^2 \rangle$ over the same itineraries and found slow but fairly good convergence throughout the chaotic regions.

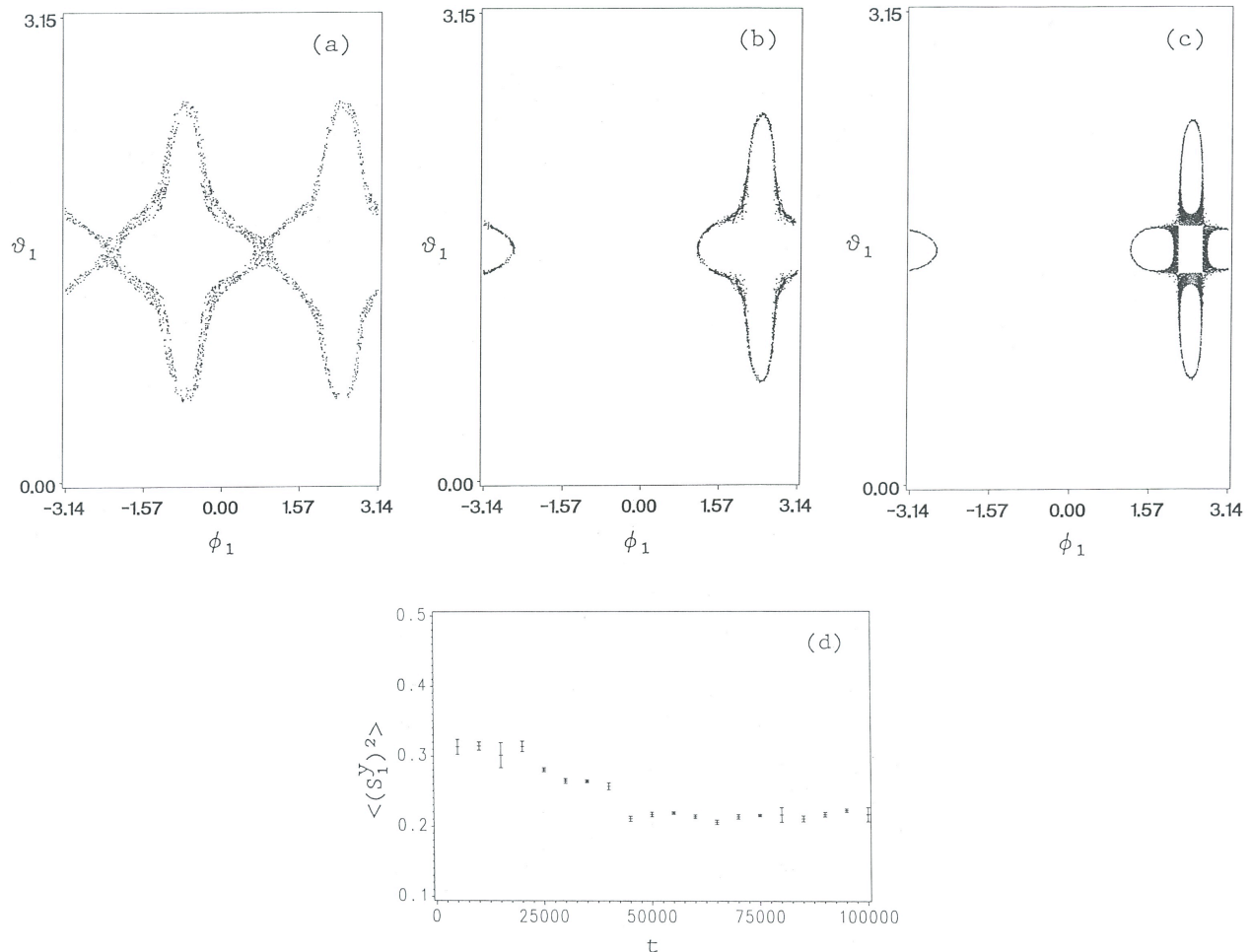


FIG. 9: Poincaré cut ($\vartheta_2 = \pi/2, \dot{\vartheta}_2 > 0$) of a chaotic itinerary on three successive time intervals: (a) $0 < t < 15000$, (b) $25000 < t < 40000$, (c) $40000 < t < 75000$. The average $\langle (S_1^y)^2 \rangle$ over successive time intervals of length $\Delta t = 5000$ for that itinerary are shown in (d).

In summary, we have observed three types of convergence in the determination of nonanalytic invariants via the numerical evaluation of time averages along itineraries:

- (i) In regions of phase space where regular trajectories are predominant, time averages converge well over time intervals of manageable size. Convergence is not significantly slower for chaotic itineraries, which are severely constrained in these regions.
- (ii) In regions of widespread chaos, the dominant mechanism which slows down the convergence of time averages is the stickiness of its boundaries. The

boundary between a chaotic region and a regular region typically consists of layers of cantori separated by regular-island chains, in which itineraries get trapped temporarily. We have found that the slowing-down of convergence due to this mechanism is considerable but not alarming, at least for the cases investigated in this study.

- (iii) A different mechanism, which is responsible for much stronger long-time anomalies, occurs in situations where a chaotic region is tessellated by cantori into roughly equal-sized compartments. A characteristic feature of this case is that time averages ap-

pear to converge slowly to some mean value, similar to case (ii), but then suddenly start to converge toward a different value [again slowly like in case (ii)], followed by an irregular sequence of further abrupt changes, each one caused whenever the itinerary switches compartment through one of the low-flux cantori. The time scales of this process are so large and widespread that the overall convergence is extremely slow.

There can be no doubt that these long-time anomalies which we have identified in simple time averages must play a prominent role in dynamic correlation functions. In the context of area-preserving maps it was already found that the stickiness of the boundaries of chaotic regions gives rise to time-dependent correlation functions

with slow algebraic decay [22-24]. We have preliminary results which indicate that the same is true for correlation functions of classical two-spin clusters in regions of widespread chaos. A detailed study of dynamic correlation functions of integrable and nonintegrable classical and quantum spin clusters is currently in progress.

Acknowledgments

The research at URI was supported by a Grant from Research Corporation and by the U.S. National Science Foundation, Grant No. DMR-86-03036. The research in Basel was supported by the Swiss National Science Foundation.

-
- [1] Magyari, E., Thomas, H., Weber, R., Kaufman, C., Müller, G.: *Z. Phys. B-Condensed Matter* **65**, 363 (1987).
- [2] Preliminary results of the present study have appeared in conference proceedings: Srivastava, N., Kaufman, C., Müller, G., Magyari, E., Weber, R., Thomas, H.: *J. Appl. Phys.* **61**, 4438 (1987).
- [3] *Chaotic behavior in quantum systems: theory and applications*. Casati, G. (ed.). New York: Plenum Press 1985.
- [4] Müller, G.: *Phys. Rev. A* **34**, 3345 (1986).
- [5] *Magneto-structural correlations in exchange coupled systems*. Willett, R.D., Gatteschi, D., Kahn, O. (eds.). Boston: Reidel 1985.
- [6] Kent, T.A., Huynh, B.H., Münck, E.: *Proc. Natl. Acad. Sci. USA* **77**, 6674 (1980) Girerd, J.J., Papaefthymiov, G.C., Watson, A.D., Gamp, E., Hagen, K.S., Edelstein, N., Frankel, R.B., Holm, R.H.: *J. Am. Chem. Soc.* **1984**, 5941 (1984).
- [7] De Jongh, L.J. in [5] p. 1.
- [8] N independent integrals of the motion in involution can be chosen as follows: $I_1 = \sum_{l'} S_{l'}^z$, $I_l = \mathbf{S}_l \cdot (\mathbf{S}_1 + \mathbf{S}_2 + \dots + \mathbf{S}_{l-1})$, $l = 2, \dots, N$. Note that the set of invariants given in (III.49) of [1] are, in fact, not all in involution.
- [9] In several cases the nonintegrability of these clusters has been verified numerically.
- [10] Nakamura, K., Bishop, A.R.: *Phys. Rev. B* **33**, 1963 (1986).
- [11] Nevertheless, for all initial conditions on the special energy hypersurface $E = 0$, the azimuthal spin motion is absent: $\dot{\phi}_1 = \dot{\phi}_2 \equiv 0$, and the remaining meridional motion is periodic, again expressible in terms of Jacobi elliptic functions.
- [12] In some regions of phase space there is more than one value $\phi_2^{(0)}$ for given values of $\vartheta_1^{(0)}, \vartheta_2^{(0)}, \phi_1^{(0)}$ and E ; in other regions there is no value at all. For the construction of Fig. 3 (and also of Fig. 4) it is important to ensure that all the values of $\phi_2^{(0)}$ chosen result in trajectories which are located (in the Poincaré cut) on the same sheet of the energy surface projected onto the (ϑ_1, ϕ_1) plane.
- [13] There appears to be no simple symmetry consideration leading to an exact determination of the periodic trajectories associated with the two elliptic fixed points in Fig. 3(b). In any event, our numerical calculation of these periodic trajectories do not seem to give us the clue to an analytic solution. They merely tell us that S_2^z and ϕ_2 are odd functions of S_1^z, ϕ_1 , respectively, with $S_1^z S_2^z \leq 0$ and $\phi_1 \phi_2 \leq 0$.
- [14] In fact, the elliptic fixed point in Fig. 4(a) corresponds to a periodic trajectory of symmetry PC_2^x and the hyperbolic fixed point to one of symmetry PC_2^y .
- [15] Cantori are invariant Cantor sets. Under the influence of an increasing nonintegrable perturbation (in our case, α increasing from zero), invariant tori with irrational frequency ratios are not immediately destroyed like their rational counterparts. However, at some threshold of the nonintegrable perturbation, an irrational torus starts to degenerate into a Cantor set while it retains its invariant character but loses the property of being an impenetrable barrier to the chaotic phase flow. Nevertheless, the phase flow through the infinitely many holes of a cantorus can be extremely weak.
- [16] This property does, of course, not hold for isolated periodic trajectories within chaotic regions such as the ones represented by the primary hyperbolic fixed points in Fig. 4(a) and (b).
- [17] Depending on the number of decimal places used in the numerical integration.
- [18] Combined with an increasing number of digits used in the execution of the $RK4[dt]$ integration.
- [19] Only if the time step of the chaotic itinerary is chosen unreasonably large do we find the unphysical phenomenon that a chaotic itinerary turns into a regular one at some point along the way. Once turned regular, the exponential error propagation disappears and the regular itinerary is stable. Under such circumstances, one might say that regular itineraries act effectively like attractors. However, for reasonably small time steps we have not observed this phenomenon in our calculations. A likely mechanism which prevents this from happening is that as a chaotic itinerary approaches an invariant torus the rate of exponential error propagation becomes smaller, so small that the error is always too small to allow it to jump onto the torus. A similar phenomenon was described previously by Chirikov, B.V., Izraelev, F.M.: *Physica* **2D**, 30 (1981) and Chirikov, B.V., Shepalyansky, D.L.: *Physica*

- 13D**, 395 (1984). They discuss the capture of chaotic trajectories by regular regions under the influence of weak dissipation.
- [20] Khinchin, A.I.: *Mathematical foundations of statistical mechanics*, p. 19. New York: Dover 1949; Abraham, R., Marsden, J.E.: *Foundation of mechanics*, 2nd ed., p. 238. Reading: Benjamin/Cummings 1985.
- [21] Since the dashed line in Fig. 3(c), on which the initial conditions used for Fig. 6 are equally spaced, is, in fact, the projection of a curved line on the energy surface in 3D $(\vartheta_1, \phi_1, \phi_2)$ -space, additional singularities in the curves of Fig. 6 may be caused by points where the line of initial conditions has infinite slope with respect to the projection plane.
- [22] Chirikov, B.V., Shepalyanski, D.L.: *Physica* **13D**, 395 (1984).
- [23] Hanson, J.D., Cary, J.R., Meiss, J.D.: *J. Stat. Phys.* **39**, 327 (1985).
- [24] Meiss, J.D., Ott, E.: *Physica* **20D**, 387 (1986).